



Geophysical Research Letters[®]

RESEARCH LETTER

10.1029/2024GL112922

Key Points:

- Solar wind magnetic field ULF fluctuations (2–8 mHz) increase energy transfer at the magnetopause boundary and into the inner magnetosphere
- The upstream fluctuations regulate the lobe dynamics and plasma flows at the magnetotail neutral current sheet
- The varying lobe and nightside dynamics are reflected in ground indices with solar wind fluctuations driving a stronger geomagnetic response

Supporting Information:

Supporting Information may be found in the online version of this article.

Correspondence to:

M. Ala-Lahti,
mattali@umich.edu

Citation:

Ala-Lahti, M., Pulkkinen, T. I., Brenner, A., Keebler, T., Al Shidi, Q., Hill, S., & Welling, D. (2024). The Impact of solar wind magnetic field fluctuations on the magnetospheric energetics. *Geophysical Research Letters*, 51, e2024GL112922. <https://doi.org/10.1029/2024GL112922>

Received 9 OCT 2024

Accepted 20 NOV 2024

The Impact of Solar Wind Magnetic Field Fluctuations on the Magnetospheric Energetics

Matti Ala-Lahti^{1,2} , Tuija I. Pulkkinen¹ , Austin Brenner¹ , Timothy Keebler¹ , Qusai Al Shidi³ , Shannon Hill^{1,4} , and Daniel Welling¹

¹Department of Climate and Space Sciences and Engineering, University of Michigan, Ann Arbor, MI, USA, ²Department of Physics, University of Helsinki, Helsinki, Finland, ³West Virginia University, Morgantown, WV, USA, ⁴University of Iowa, Iowa City, IA, USA

Abstract Solar wind drives magnetospheric dynamics through coupling with the geospace system at the magnetopause. While upstream fluctuations correlate with geomagnetic activity, their impact on the magnetopause energy transfer is an open question. In this study, we examine three-dimensional global magnetospheric simulations using the Geospace configuration of the Space Weather Modeling Framework. We examine the effects of solar wind fluctuations during a substorm event by running the model with four different driving conditions that vary in fluctuation frequency spectrum. We demonstrate that upstream fluctuations intensify the energy exchange at the magnetopause increasing both energy flux into and out of the system. The increased energy input is reflected in ground magnetic indices. Moreover, the fluctuations impact the magnetopause dynamics by regulating the energy exchange between the polar caps and lobes and energy transport within the magnetotail neutral sheet.

Plain Language Summary Earth's magnetic field shields the near-Earth space plasma environments from the direct influence of solar wind. Solar wind however drives the magnetosphere when physical processes at the magnetopause boundary enable the transfer of energy between the plasmas. The coupling has global consequences in the magnetosphere system and its efficiency is particularly dependent on the orientation of interplanetary magnetic field and its magnitude but also on magnetic field fluctuation power. We capture the impact of upstream fluctuations on magnetopause energy exchange and nightside magnetotail dynamics by analyzing magnetohydrodynamic simulations of the global magnetosphere using various upstream driving conditions. We discover that more energy flows out from and into the system at the magnetopause when the upstream solar wind plasma include magnetic field fluctuations. The upstream fluctuation power is moreover reflected in nightside magnetotail, where flow patterns at the neutral sheet are regulated, as well as to ground indices with fluctuations driving a stronger geomagnetic response.

1. Introduction

Magnetospheric phenomena are driven by the solar wind interaction at the magnetopause boundary. The physical processes that enable transfer of energy between the solar wind and Earth's magnetosphere (Burton et al., 1975; Weigel et al., 2003) have global consequences including substorms during which energy is released earthward from the nightside magnetotail (Hones, 1979).

While the orientation and magnitude of interplanetary magnetic field (IMF) control the strength of the coupling, the field fluctuations are also correlated with magnetospheric phenomena. Ultralow frequency (ULF; mHz) waves in the solar wind increase auroral activity (Borovsky & Funsten, 2003; D'Amicis et al., 2007, 2009), both during southward and northward IMF (Osmane et al., 2015). The response at low latitudes is, however, ambiguous (Wanliss & Weygand, 2007; D'Amicis et al., 2010, 2011; Alimaganbetov & Streltsov, 2020). It is still unknown through which processes the upstream fluctuations increase geomagnetic activity (Borovsky, 2021).

Only a few studies have quantitatively addressed the net energy transfer through the magnetopause (Ala-Lahti et al., 2022; Brenner et al., 2021, 2023). These studies show net energy outflow from the magnetosphere in the dayside and inflow through the tail lobes (see also Palmroth et al., 2003, 2006, 2010, 2011). Prior numerical studies have examined the magnetospheric impact of solar wind dynamic pressure fluctuations (Claudepierre et al., 2010; Zhou et al., 2022), synthetic Alfvénic waves (McGregor et al., 2014) and background solar wind

© 2024, The Author(s).

This is an open access article under the terms of the [Creative Commons Attribution License](#), which permits use, distribution and reproduction in any medium, provided the original work is properly cited.

averaged to frequencies 0.2 mHz (Ilie et al., 2010). The impact of the solar wind fluctuations on the energy transfer, however, has thus far not been quantified.

Here we investigate the importance of solar wind fluctuations for solar wind—magnetosphere coupling by modeling the Earth's space plasma environment with global magnetospheric simulations. We focus on the impacts during substorm intervals of solar wind ULF and sub-ULF (<1 mHz) fluctuations. Particularly, we specify the impact by computing the energy fluxes through magnetospheric boundaries and quantifying the nightside dynamics at the neutral sheet, effects that have not been examined in prior simulation analyses.

2. Methods

2.1. Space Weather Modeling Framework (SWMF)

This work uses the Space Weather Modeling Framework (SWMF) in its Geospace configuration (Tóth et al., 2012) to simulate the coupled solar wind-global magnetosphere-ionosphere system. The Geospace configuration consists of the outer magnetosphere, inner magnetosphere and ionosphere electrodynamics components, with Block Adaptive Tree Solar-wind Roe Upwind Scheme (BATS-R-US) (Powell et al., 1999) solving ideal MHD equations to model solar wind. The magnetosphere is modeled with a varied grid resolution that ranges from $0.125 R_E$ in near-Earth region to $8 R_E$ in distant tail. The MHD global magnetosphere physics domain is coupled with Rice Convection Model (RCM) (Toffoletto et al., 2003) and Ridley Ionosphere Model (RIM) (Ridley et al., 2006). RCM describes non-Maxwellian plasmas of the inner magnetosphere by computing bounce- and pitch-angle-averaged phase space densities for protons, electrons and single charged oxygen ions, whereas RIM solves the Poisson equation for electrostatic potential distribution at a two-dimensional ionospheric surface. Ionospheric conductances for RIM are provided by Conductance Model for Extreme Events (CMEE) (Mukhopadhyay et al., 2020).

The inner magnetosphere ring current dynamics is included in the MHD solution by nudging the MHD plasma pressure and density to correspond to the RCM values, which are computed from boundary field and plasma conditions set by BATS-R-US (de Zeeuw et al., 2004). RIM on the other hand receives field-aligned currents from BATS-R-US to determine ionospheric conductances and update electric potential and field, which are then fed to the MHD model and RCM, respectively. RCM uses the electric field to compute the drift speeds.

Similar to Brenner et al. (2023), we capture the magnetopause with $0.5 R_E$ grid resolution inside a paraboloid that reaches from its nose at $X_{GSM} = 20 R_E$ ($Y_{GSM} = Z_{GSM} = 0$) to $X_{GSM} = -32 R_E$ ($Y_{GSM} = Z_{GSM} = \pm 26 R_E$). All simulation results are shown in Geocentric Solar Magnetospheric (GSM) coordinates at 1 min temporal cadence. We increase the resolution to $0.125 R_E$ within $-20 < X_{GSM} < 8$ and $-8 < Y_{GSM}, Z_{GSM} < 8 R_E$ to resolve the nightside magnetotail dynamics (see Figure S1 in Supporting Information S1). The inner boundary of the simulation domain is at $2.5 R_E$ and the simulation time step the order of 10^{-2} s (Ala-Lahti et al., 2024).

2.2. Boundary Energy Fluxes

We apply previously developed methods to identify magnetospheric boundaries and to compute boundary energy fluxes. Following Brenner et al. (2021), we use magnetic field line topology and modified plasma beta (β^*) to determine the magnetopause. The modified plasma beta is given as

$$\beta^* = 2\mu_0(P_{th} + P_{dyn})/B^2, \quad (1)$$

where μ_0 is vacuum permeability, P_{th} and P_{dyn} are thermal and dynamics pressures, and B is magnetic field magnitude (Xu et al., 2016). On the dayside, the magnetopause is defined as the outer surface of closed field lines, whereas on the nightside the magnetopause is defined as an isosurface of $\beta^* = 0.7$, which has been shown to well separate the dense magnetosheath (high thermal/dynamic pressure) from the empty tail lobes (low thermal/dynamic pressure) (Brenner et al., 2021). A tailward closure of the boundary is specified by a cutoff plane at given X_{GSM} that is adjusted to omit any solar wind field lines. The final magnetopause boundary encloses the magnetospheric volume consisting of closed and open field topologies out to the cutoff plane. In this work, we set the tail cutoff at $X_{GSM} = -40 R_E$. The energy analysis volume is further limited to outside a sphere of $r = 4 R_E$ radius; note that this boundary is different from the simulation inner boundary which resides at $2.5 R_E$.

We compute the total energy flux (\mathbf{K}) that includes the Poynting flux (\mathbf{S}) carrying electromagnetic energy and hydrodynamic energy flux (\mathbf{H}). The total energy flux can be written in the MHD limit as

$$\mathbf{K} = \mathbf{S} + \mathbf{H} = \left(\frac{B^2}{\mu_0} \mathbf{V} - \frac{\mathbf{B} \cdot \mathbf{V}}{\mu_0} \mathbf{B} \right) + \left(\frac{1}{2} \rho V^2 + \frac{\gamma}{\gamma - 1} P_{th} \right) \mathbf{V}, \quad (2)$$

where \mathbf{V} is the MHD bulk velocity, ρ the mass density, and $\gamma = 5/3$ is the ratio of specific heats. At a given boundary, the flux transfer is obtained locally as the normal component of the flux ($\mathbf{K} \cdot \mathbf{n}$), and the total energy flux rate is obtained by integrating over the boundary surface area ($\int_A \mathbf{K} \cdot d\mathbf{A}$). We use an outward sign convention, where $\mathbf{K} \cdot \mathbf{n} > 0$ indicates energy escape from the magnetosphere into the magnetosheath.

We further investigate the energy flow between the portion of the close field volume connected to the magnetosheath, and between the open lobes and the boundary at $r = 4 R_E$. Additionally the closed field is divided into dayside and nightside regions based on the average flux tube X position ($X > 0$ dayside). The boundary identification and flux calculation methods have been demonstrated and validated by Brenner et al. (2021, 2023).

2.3. Substorm 18 May 2015 and Simulation Runs

We analyze a substorm event on 18 May 2015 that had minimum AL index of -423 nT with only a minor ring current enhancement. We ran the SWMF Geospace simulation using the solar wind measured by the Wind spacecraft as upstream boundary condition. We constructed three additional runs by filtering the Wind data: First, the Wind magnetic field and plasma data were low-pass filtered to frequencies < 1 mHz. Second, we created a “box”-filtered data series, which comprises constant solar wind and IMF but stepwise varying B_Z changing only when the field turned southward/northward. Third, we extracted magnetic field ULF fluctuations (2–8 mHz; periods of 2 and 8 min) (e.g., McGregor et al., 2014; Osmane et al., 2015; Villante et al., 2022) from the original Wind observations and added that to the box-filtered time series, which yields an IMF profile that has ULF fluctuations but no lower-frequency field variations. The latter two are referred to as the “Box” and “Box + ULF” runs.

The simulations were performed from 23:00 UT on 17 May 2015 to 17:00 UT on 18 May 2015 using SWMF restart option. The magnetosphere was first initiated by driving it with the solar wind data from 23:00 UT on 17 May to 07:00 UT on 18 May 2015. The four simulations with different solar wind input data series were then run from the end state of this initiation period to 17:00 UT on 18 May 2015.

Figure 1 introduces the upstream solar wind data of the four simulation runs; the restart time is marked by the dashed vertical line, before which all simulations are identical. Figure 1a shows the unfiltered (“Orig SW” colors) and low-pass filtered (“Lowpass” black) magnetic field data from Wind. The box-filtered magnetic field with (colors) and without (black) ULF fluctuations are shown in Figure 1b. Panels 1c–d show the plasma velocity, and panels 1e–f both the number density (blue) and temperature (yellow). The dotted vertical lines delimit the southward ($B_Z < 0$) IMF period.

The Newell coupling function (Newell et al., 2007), which estimates the rate of increase of open magnetic flux from dayside reconnection, is shown in Figures 1g and 1h. The panels show both the instantaneous coupling function and its cumulative value starting from 07:00 UT on 18 May 2015. The run with higher fluctuation power in each panel is represented by the colored traces. While upstream fluctuations result in rapid variations of the Newell function, the cumulative function show only minor differences.

Figures 1i and 1j show the observed and simulated SYM-H and AL indices. The low ring current activity is demonstrated by the SYM-H values above -19 nT. The simulation with the Wind solar wind data (Orig SW) follows the observations well, but underpredicts the observed substorm-time activity. The ring current develops in the simulation with a delay, but the start of the substorm growth phase and the ending of its recovery phase match the observations well (Figure 1j).

The coupling function increases in a steplike fashion when the upstream field turns southward (first dotted line). The Newell function (Newell et al., 2007) and AL index indicate that, by the time of IMF northward turning (marked by the second dotted line) the coupling function decreased and the substorm cycle completed its recovery

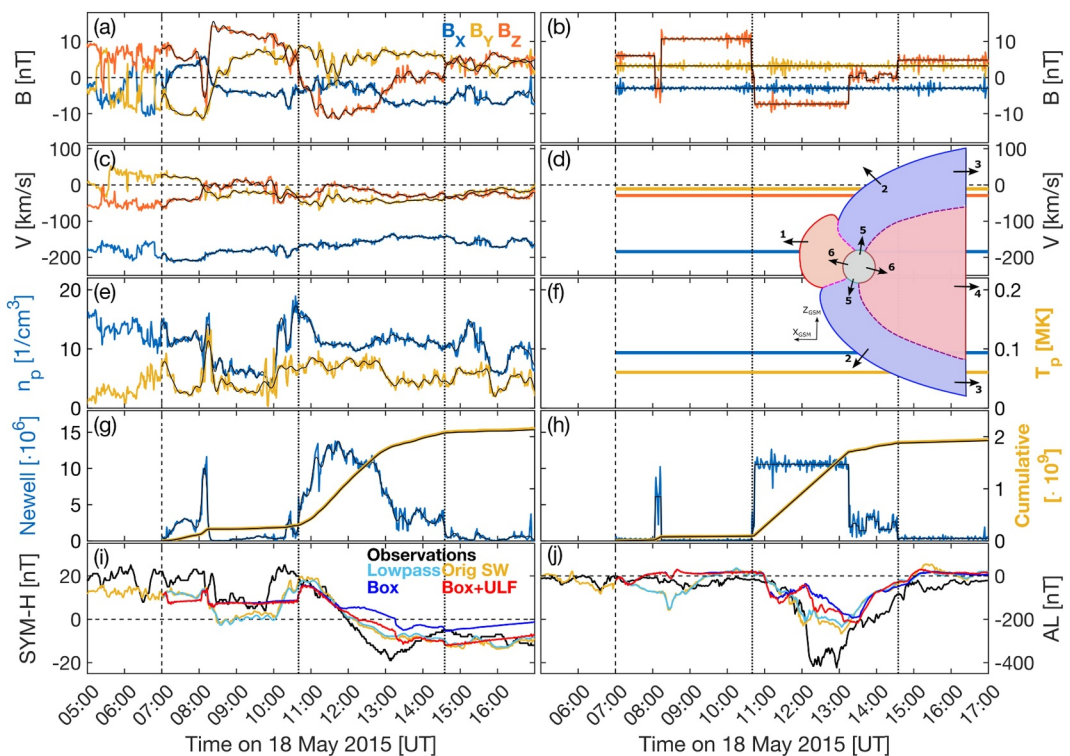


Figure 1. Simulation upstream solar wind conditions (Left: Orig SW, Lowpass; Right: Box, Box + ULF). **Panels a–f:** (a–b) Upstream magnetic field (colors - Orig SW, Box + ULF; black - Lowpass, Box), (c–d) plasma velocity (e–f) density (blue) and temperature (yellow). **Panels g–h:** Newell coupling function (blue) and its cumulative (yellow). **Panels i–j:** Geomagnetic SYM-H and AL indices, with the observations (black; OMNIWeb). **Inset:** Schematic of magnetospheric boundary fluxes in the noon-midnight meridional plane. Flux through the outer boundary is given by fluxes 1–4. The inner solid lines (teal and brown) illustrate the inner boundary at $r = 4 R_E$ (fluxes 5–6). Purple - open field line regions; red - closed field line regions.

phase. We refer to the interval bounded by the dotted lines as the event and mark these times in all subsequent figures.

The simulation results imply that upstream fluctuations increase the magnetospheric response during disturbed period. The AL index diverges during the substorm differing by $\sim 20 - 50$ nT between the Orig SW and Lowpass runs. This effect is more distinct between the Box + ULF and Box runs (20–80 nT), which also show a long-lasting difference in SYM-H. Before the event, no significant differences are observed between the two pairs of traces with and without ULF waves. The AL curves converge in the substorm recovery phase.

Next we examine whether these differences can be traced to variations of the energy flux at the magnetosphere boundaries. The surfaces and their boundary normal directions are shown in the insert embedded in Figure 1. The total flux into and out from the geoeffective portion of the magnetosphere (bounded by the magnetopause and the tail cut plane; hereafter referred to as “outer boundary”) is given by fluxes 1–4, and through the boundary at $r = 4 R_E$ (hereafter referred to as “inner boundary”) by fluxes 5–6. Note that flux 1 includes also flux through the closed field line boundary extending into the nightside at the flanks of the magnetotail. We denote the fluxes K1–K6, where K refers to the total energy flux (see Equation 2).

3. Results—Energy Flux Through the System Boundaries

The total energy flux through the magnetospheric outer boundary (the sum of K1–K4) and the inner boundary (K5–K6) are shown in Figure 2. Figures 2c and 2d show the total flux as the sum of the outward ($\mathbf{K} \cdot \mathbf{n} > 0$) and inward flux components ($\mathbf{K} \cdot \mathbf{n} < 0$) shown with the pale lines only during the event period (see also Table S1 in Supporting Information S1). It is clear that at any given time, the net energy transport is a small fraction of the

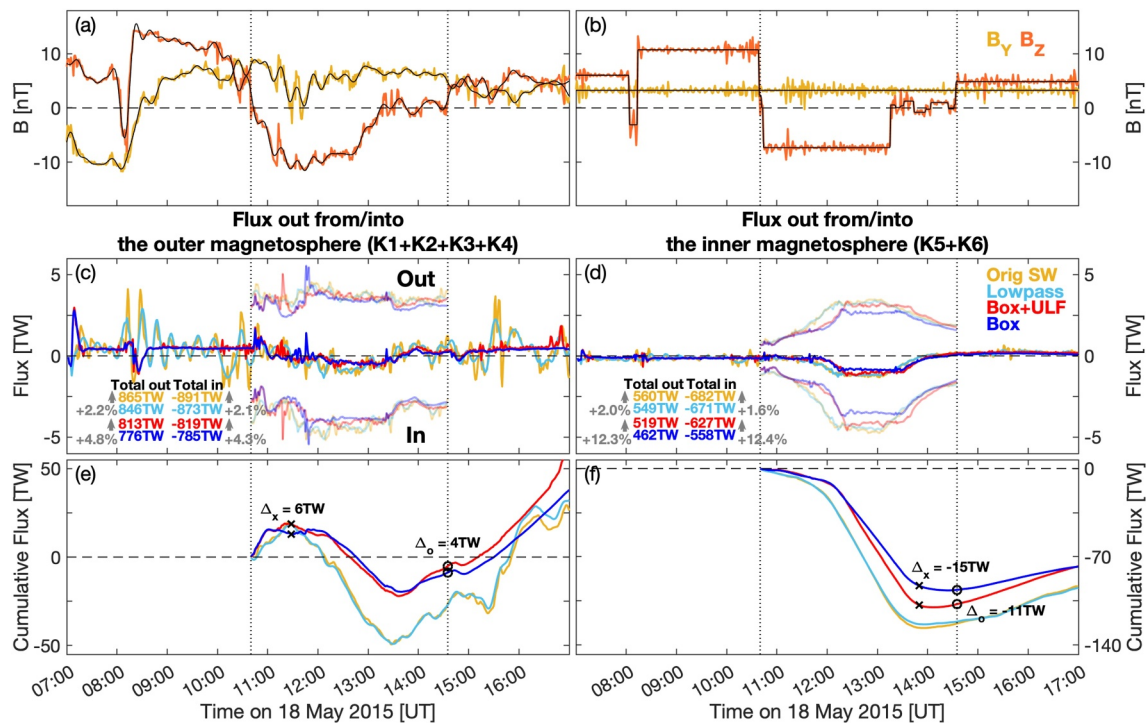


Figure 2. Magnetospheric bulk fluxes and their cumulatives. **Panels a–b:** Upstream B_y and B_z . **Panels c–d:** Total energy flux through the outer boundary and inner boundary at $r = 4R_E$. Escape (out) and entry (in) are plotted over the event in pale colors; their integral values are given in the insert. **Panels e–f:** Cumulative of the total energy flux shown in panels c–d.

inward and outward transport that roughly balance each other. The results at the outer boundary show that southward IMF results in net energy input into the system (negative total flux values in Figure 2c).

The impact of the upstream fluctuations on solar wind–magnetosphere coupling is seen by comparing the yellow and red curves with their low-pass counterparts shown in cyan and blue, respectively. Integrating the negative and positive values over the event shows that the solar wind fluctuations intensified the inward and outward energy exchange, but did not have a major impact on the net energy flux (total flux out + total flux in $\sim \text{const}$: Orig SW/Lowpass:-26/ – 27 TW; Box + ULF/Box:-6/–9 TW).

Figure 2d shows that, similar to the outer boundary, the solar wind fluctuations increased fluxes both out from and into the inner magnetosphere and ionosphere through the inner boundary. While the Orig SW and Lowpass runs show no marked differences during the event, in the Box + ULF run the upstream fluctuations resulted in a more significant increase in the active time energy exchange. Interestingly, this increase is not comparable to the changes at the outer boundary (inner boundary +12.3% vs. outer boundary +4.3%). This suggests that the fluctuations are important in regulating the inner magnetosphere and magnetotail dynamics. We note that the flux in Figure 2d is dominated by the K6 flux (see Figure S2 in Supporting Information S1).

The cumulative of the total (in + out) energy flux through the outer and inner boundary is shown in Figures 2e and 2f. In panel e, all curves show negative values at 14:35 UT implying that the magnetosphere experienced total energy gain during the examined time interval. Matching yellow and cyan curves demonstrate similar outer boundary dynamics between the Orig SW and Lowpass runs. The red and blue curves on the other hand diverge over time suggesting slightly varying dynamics between the Box + ULF and Box runs. First, the curves show minor differences before steady energy input into the magnetosphere indicated by a negative slope starts at 12:05. Second, based on the higher positive slope of the red curve at the end of the event, the fluctuations boosted system energy loss. The cumulative fluxes of Box + ULF and Box runs, furthermore, diverged at the inner boundary (Figure 2f).

Next we focus on the fluxes through the closed field line outer boundary and the open field line inner boundary (K1, K4 and K5 fluxes, see Figure 1 insert; see also Figure S2 in Supporting Information S1). Figure 3a shows the total K1 flux (strong colors) and its inward and outward components (light colors) on the dayside, with Figure 3b

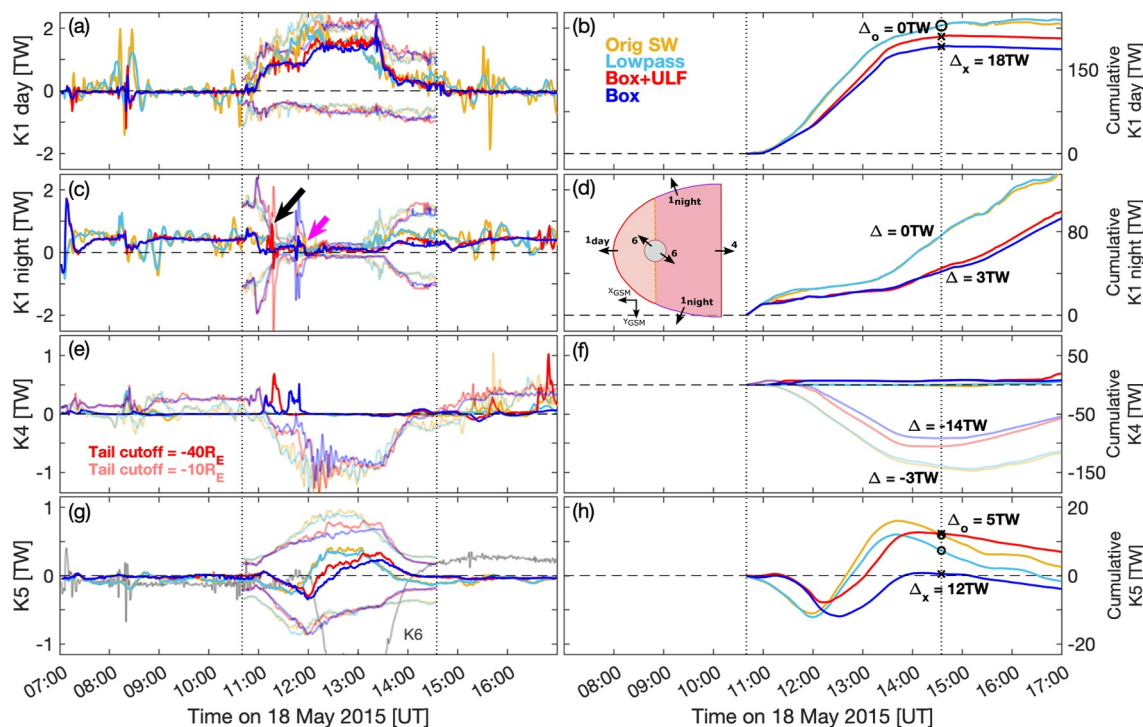


Figure 3. Magnetospheric energy fluxes shown in the format of Figure 2. **Panels a–b:** Dayside K1 flux. **Panels c–d:** Nightside K1 flux. **Panels e–f:** K4 flux at $X = -40 R_E$ and at $X = -10 R_E$ (light lines). **Panels g–f:** K5 flux and the total K6 flux from the Box + ULF run. K6 flux is shown to illustrate the magnitude differences between K5 and K6 (see Figure 2d). **Inset:** Schematic of magnetospheric boundary fluxes in the equatorial plane.

showing the cumulative of the total flux. Similar to prior numerical work (Ala-Lahti et al., 2022; Brenner et al., 2021, 2023), the energy flows out from the magnetosphere through the dayside magnetopause during southward IMF as magnetic reconnection erodes the terrestrial magnetic flux. Based on the results from the Box + ULF versus Box runs, solar wind IMF fluctuations at 2–8 mHz frequencies can enhance the dayside flux erosion.

Figures 3c and 3d show the nightside K1 flux. The black arrow marks a spike in the Box + ULF run, which was traced to tailward of $X = -20 R_E$ and was completely absent in the Box run. Both runs included another distinct flux spike (magenta arrow). This fluctuation occurred between $X = -20$ and $-40 R_E$ in the Box run but earthward of $-20 R_E$ in the Box + ULF run. The total flux over the event, however, did not drastically differ between the runs (Figure 3d). This observation supports the earlier discussion on Figure 2e that the upstream fluctuations can alter magnetopause boundary dynamics: Even if the total energy exchange during an event did not vary significantly, the upstream conditions affect the time-history of solar wind–magnetosphere coupling as well as the exact location where energy is exchanged between the plasma regimes.

This effect is also seen in Figure 3e, where the tail cutoff closed K4 flux at $X = -40$ shows differences between the Box + ULF and Box runs while the total flux over the event remains the same (Figure 3f). As the K4 flux is the flux through the closed magnetotail at the cutoff distance, its negligible values imply that nightside reconnection happens earthward of $X = -40 R_E$. The light-colored lines in Figures 3e and 3f show K4 when the tailward boundary was placed at $X = -10 R_E$. The fluxes are earthward (negative), highly fluctuating and their temporal variations do not agree. The cumulative values (Figure 3f) show however that the differences between the Orig SW and Lowpass runs are marginal.

The K5 flux between the lobes and polar caps differ between the simulations. At the event beginning, all runs showed energy flow from the lobes to the polar caps (negative flux values; Figure 3g). While the energy flux changed to flow from the polar caps into the lobes (positive total values) simultaneously in the Orig SW and Lowpass runs, the change in the direction happened at different times between the Box and Box + ULF runs. In

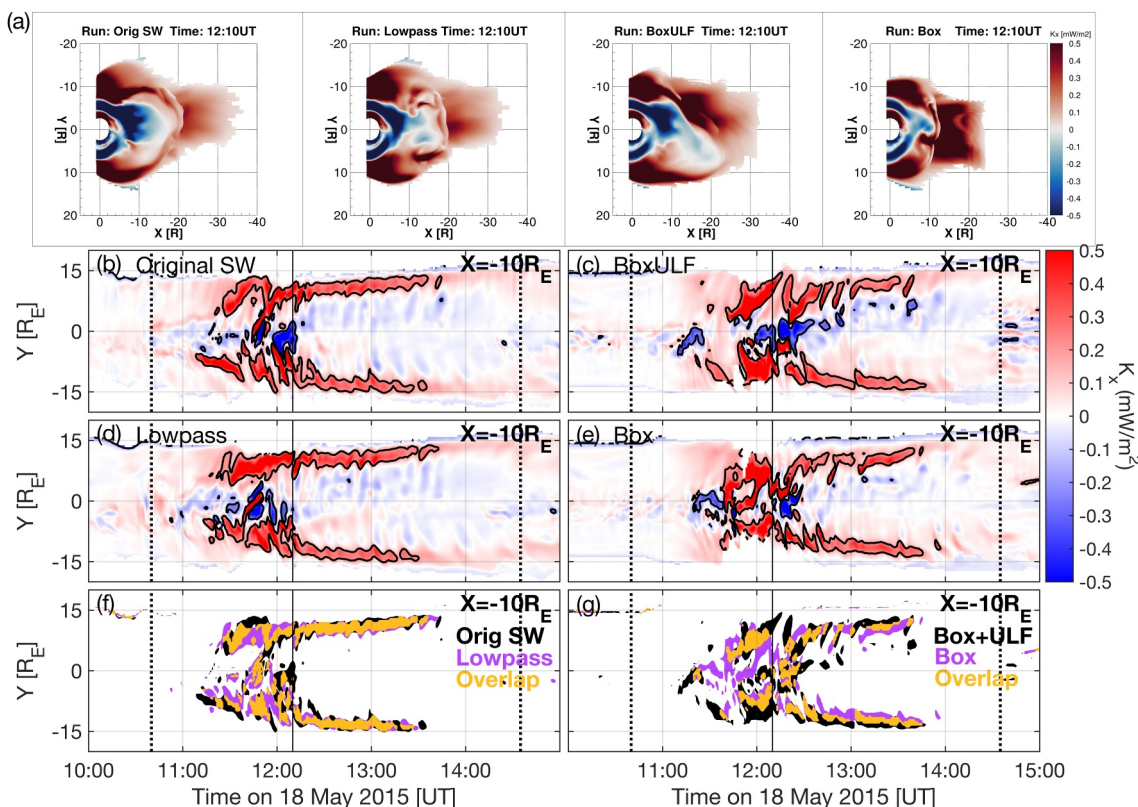


Figure 4. Energy flux within the magnetotail neutral sheet. **Panel a:** X-component of the total energy flux captured at the magnetotail neutral sheet at 12:10UT. The neutral sheet is defined as $B_R = 0$ within the closed field line topology. **Panel b–e:** Neutral sheet K_x extracted at $X = -10 R_E$, with the contours demarcating values $|K_x| > 0.2 \text{ mW/m}^2$. **Panel f–g:** The contoured areas from panels b–e (black—Orig SW and Box ULF; purple—Lowpass and Box). The yellow indicates the areas where the contours overlap.

addition, the energy flux into the polar caps was larger during steadier solar wind conditions (see the curve minima in Figure 3h).

Because of these differences, the positive cumulative flux at the end, that is, lobes experiencing net energy input, was reached earlier and it was more substantial in the runs with upstream fluctuations. Most strikingly, the Box run showed no net energy gain/loss during the event.

Finally, we examine nightside magnetotail dynamics. We focus on the X-component of the total energy flux (K_x) at the neutral sheet defined as the surface where the radial magnetic field component vanishes ($B_r = 0$) (Palmroth et al., 2023) within closed field region. Figure 4a shows how the four simulations captured different energy flow patterns as well as neutral sheet shape in terms of tailward extent (along X) and width (in Y direction).

We further extract the time series of K_x at the neutral sheet at $X = -10 R_E$. The results are shown for the four runs in Figures 4b–4e, with the contours demarcating fluxes above and below $\pm 0.2 \text{ mW/m}^2$. In Figures 4f and 4g, the contoured high-transport areas are shown in the same plot for comparison (black—Orig SW, Box + ULF; purple—Lowpass, Box; yellow—overlap). Both comparisons show largest differences at the beginning of the event and at the midnight sector neutral sheet ($Y = 0 R_E$).

4. Conclusions

Our results indicate that the presence of solar wind IMF ULF fluctuations (2–8 mHz) determine a stronger geomagnetic activity. While prior work has shown that upstream ULF fluctuations intensify solar wind–magnetosphere coupling, especially auroral activity (e.g., Borovsky & Funsten, 2003; Borovsky, 2023; D’Amicis et al., 2007; Osmane et al., 2015), this is the first study to quantitatively assess the energy transport globally throughout the magnetopause boundary and through a cross-section of the tail. The connection between

solar wind fluctuations and low-latitude (SYM-H) response is however more ambiguous (Wanliss & Weygand, 2007; D'Amicis et al., 2010, 2011; Alimaganbetov & Streltsov, 2020), and further studies focusing on the impact during geomagnetic storms ought to be constructed.

In this study, energy exchange at the system boundaries increased with upstream fluctuation power. Interestingly, the increase at the inner boundary (energy flux into and out of the polar caps and inner magnetosphere) was much larger than the increase at the outer boundary between the Box + ULF and Box runs. While this effect was absent in the Orig SW and Lowpass comparison, the dynamics at the neutral sheet varied based on the solar wind conditions, with upstream fluctuations increasing earthward energy flux on the nightside (Figure 3f).

We observed that solar wind conditions regulate the magnetopause boundary dynamics, particularly where and when energy is transferred at the system outer boundary. These results are consistent with prior MHD simulations that show upstream solar wind Alfvénicity enhancing Kelvin-Helmholtz instability (McGregor et al., 2014). In this study, dayside flux erosion was enhanced during IMF ULF fluctuations, which may result from regulated dayside boundary dynamics including varying reconnection rates and multiple X-lines (e.g., Hoilijoki et al., 2017; Raeder, 2006). Also the energy transfer between the lobes and polar caps was sensitive to upstream conditions.

These findings highlight the nonlinearity of solar wind—magnetosphere coupling (D'Amicis et al., 2020), but more focused studies are required to understand causalities and consequences in the inner magnetosphere. For example, the dynamics associated with magnetosphere lobes acting as energy reservoirs (Baker et al., 1996; Brenner et al., 2023) could well be addressed by global numerical simulations.

Data Availability Statement

The simulations were constructed with the Space Weather Modeling Framework (SWMF) and BATS-R-US tools developed at and made available for download by the University of Michigan. The analyzed simulation and upstream solar wind data as well as the simulation software and analysis tools are available at and via Ala-Lahti et al. (2024).

Acknowledgments

MA-L and TP were supported through and acknowledge the NSF Grant 2033563 and 2420675, and NASA Federal Award 80NSSC23M0192.

References

Ala-Lahti, M., Pulkkinen, T. I., Brenner, A., Keebler, T., Al Shidi, Q., Hill, S., & Welling, D. (2024). The impact of solar wind magnetic field fluctuations on the magnetospheric energetics. *Zenodo*. [Dataset]. <https://doi.org/10.5281/zenodo.14170898>

Ala-Lahti, M., Pulkkinen, T. I., Pfau-Kempf, Y., Grandin, M., & Palmroth, M. (2022). Energy flux through the magnetopause during flux transfer events in hybrid-vlasov 2D simulations. *Geophysical Research Simulations*, 49(19), e2022GL100079. <https://doi.org/10.1029/2022GL100079>

Alimaganbetov, M., & Streltsov, A. V. (2020). ULF waves observed in solar wind and on the ground at high, mid, and low latitudes. *Journal of Atmospheric and Solar-Terrestrial Physics*, 200, 105220. <https://doi.org/10.1016/j.jastp.2020.105220>

Baker, D. N., Pulkkinen, T. I., Angelopoulos, V., Baumjohann, W., & McPherron, R. L. (1996). Neutral line model of substorms: Past results and present view. *Journal of Geophysical Research*, 101(A6), 12975–13010. <https://doi.org/10.1029/95JA03753>

Borovsky, J. E. (2021). Perspective: Is our understanding of solar-wind/magnetosphere coupling satisfactory? *Frontiers in Astronomy and Space Sciences*, 8, 5. <https://doi.org/10.3389/fspas.2021.634073>

Borovsky, J. E. (2023). Further investigation of the effect of upstream solar-wind fluctuations on solar-wind/magnetosphere coupling: Is the effect real? *Frontiers in Astronomy and Space Sciences*, 9, 433. <https://doi.org/10.3389/fspas.2022.975135>

Borovsky, J. E., & Funsten, H. O. (2003). Role of solar wind turbulence in the coupling of the solar wind to the Earth's magnetosphere. *Journal of Geophysical Research (Space Physics)*, 108(A6), 1246. <https://doi.org/10.1029/2002JA009601>

Brenner, A., Pulkkinen, T. I., Al Shidi, Q., & Toth, G. (2021). Stormtime energetics: Energy transport across the magnetopause in a global MHD simulation. *Frontiers in Astronomy and Space Sciences*, 8, 180. <https://doi.org/10.3389/fspas.2021.756732>

Brenner, A., Pulkkinen, T. I., Al Shidi, Q., & Toth, G. (2023). Dissecting Earth's magnetosphere: 3D energy transport in a simulation of a real storm event. *Journal of Geophysical Research (Space Physics)*, 128(11), e2023JA031899. <https://doi.org/10.1029/2023JA031899>

Burton, R. K., McPherron, R. L., & Russell, C. T. (1975). An empirical relationship between interplanetary conditions and Dst. *Journal of Geophysical Research*, 80(31), 4204–4214. <https://doi.org/10.1029/JA080i031p04204>

Claudepierre, S. G., Hudson, M. K., Lotko, W., Lyon, J. G., & Denton, R. E. (2010). Solar wind driving of magnetospheric ULF waves: Field line resonances driven by dynamic pressure fluctuations. *Journal of Geophysical Research (Space Physics)*, 115(A11), A11202. <https://doi.org/10.1029/2010JA015399>

D'Amicis, R., Bruno, R., & Bavassano, B. (2007). Is geomagnetic activity driven by solar wind turbulence? *Geophysical Journal Letters*, 34(5), L05108. <https://doi.org/10.1029/2006GL028896>

D'Amicis, R., Bruno, R., & Bavassano, B. (2009). Alfvénic turbulence in high speed solar wind streams as a driver for auroral activity. *Journal of Atmospheric and Solar-Terrestrial Physics*, 71(10–11), 1014–1022. <https://doi.org/10.1016/j.jastp.2008.05.002>

D'Amicis, R., Bruno, R., & Bavassano, B. (2010). Geomagnetic activity driven by solar wind turbulence. *Advances in Space Research*, 46(4), 514–520. <https://doi.org/10.1016/j.asr.2009.08.031>

D'Amicis, R., Bruno, R., & Bavassano, B. (2011). Response of the geomagnetic activity to solar wind turbulence during solar cycle 23. *Journal of Atmospheric and Solar-Terrestrial Physics*, 73(5–6), 653–657. <https://doi.org/10.1016/j.jastp.2011.01.012>

D'Amicis, R., Telloni, D., & Bruno, R. (2020). The effect of solar-wind turbulence on magnetospheric activity. *Frontiers in Physics*, 8, 541. <https://doi.org/10.3389/fphy.2020.604857>

de Zeeuw, D. L., Sazykin, S., Wolf, R. A., Gombosi, T. I., Ridley, A. J., & Tóth, G. (2004). Coupling of a global MHD code and an inner magnetospheric model: Initial results. *Journal of Geophysical Research (Space Physics)*, 109(A12), A12219. <https://doi.org/10.1029/2003JA010366>

Hoilijoki, S., Ganse, U., Pfau-Kempf, Y., Cassak, P. A., Walsh, B. M., Hietala, H., et al. (2017). Reconnection rates and X line motion at the magnetopause: Global 2D-3V hybrid-Vlasov simulation results. *Journal of Geophysical Research (Space Physics)*, 122(3), 2877–2888. <https://doi.org/10.1002/2016JA023709>

Hones, J. E. W. (1979). Transient phenomena in the magnetotail and their relation to substorms (article published in the special issues: Proceedings of the symposium on solar terrestrial physics held in innsbruck, may- june 1978. (pp. 137–538)). *Space Science Reviews*, 23(3), 393–410. <https://doi.org/10.1007/BF00172247>

Ilie, R., Liemohn, M. W., & Ridley, A. (2010). The effect of smoothed solar wind inputs on global modeling results. *Journal of Geophysical Research (Space Physics)*, 115(A1), A01213. <https://doi.org/10.1029/2009JA014443>

McGregor, S. L., Hudson, M. K., & Hughes, W. J. (2014). Modeling magnetospheric response to synthetic alfvénic fluctuations in the solar wind: ULF wave fields in the magnetosphere. *Journal of Geophysical Research (Space Physics)*, 119(11), 8801–8812. <https://doi.org/10.1002/2014JA020000>

Mukhopadhyay, A., Welling, D. T., Liemohn, M. W., Ridley, A. J., Chakraborty, S., & Anderson, B. J. (2020). Conductance model for Extreme events: Impact of auroral conductance on space weather forecasts. *Space Weather*, 18(11), e2020SW002551. <https://doi.org/10.1029/2020SW002551>

Newell, P. T., Sotirelis, T., Liou, K., Meng, C. I., & Rich, F. J. (2007). A nearly universal solar wind-magnetosphere coupling function inferred from 10 magnetospheric state variables. *Journal of Geophysical Research (Space Physics)*, 112(A1), A01206. <https://doi.org/10.1029/2006JA012015>

Osmane, A., Dimmock, A. P., Naderpour, R., Pulkkinen, T. I., & Nykyri, K. (2015). The impact of solar wind ULF $\text{t}_{\text{ext}}\{\text{B}\}_{\{z\}}$ fluctuations on geomagnetic activity for viscous timescales during strongly northward and southward IMF. *Journal of Geophysical Research (Space Physics)*, 120(11), 9307–9322. <https://doi.org/10.1002/2015JA021505>

Palmroth, M., Koskinen, H. E. J., Pulkkinen, T. I., Toivanen, P. K., Janhunen, P., Milan, S. E., & Lester, M. (2010). Magnetospheric feedback in solar wind energy transfer. *Journal of Geophysical Research (Space Physics)*, 115(A5), A00110. <https://doi.org/10.1029/2010JA015746>

Palmroth, M., Laitinen, T. V., Anekallu, C. R., Pulkkinen, T. I., Dunlop, M., Lucek, E. A., & Dandouras, I. (2011). Spatial dependence of magnetopause energy transfer: Cluster measurements verifying global simulations. *Annales Geophysicae*, 29(5), 823–838. <https://doi.org/10.5194/angeo-29-823-2011>

Palmroth, M., Laitinen, T. V., & Pulkkinen, T. I. (2006). Magnetopause energy and mass transfer: Results from a global MHD simulation. *Annales Geophysicae*, 24(12), 3467–3480. <https://doi.org/10.5194/angeo-24-3467-2006>

Palmroth, M., Pulkkinen, T. I., Ganse, U., Pfau-Kempf, Y., Koskela, T., Zaitsev, I., et al. (2023). Magnetotail plasma eruptions driven by magnetic reconnection and kinetic instabilities. *Nature Geoscience*, 16(7), 570–576. <https://doi.org/10.1038/s41561-023-01206-2>

Palmroth, M., Pulkkinen, T. I., Janhunen, P., & Wu, C. C. (2003). Stormtime energy transfer in global MHD simulation. *Journal of Geophysical Research (Space Physics)*, 108(A1), 1048. <https://doi.org/10.1029/2002JA009446>

Powell, K. G., Roe, P. L., Linde, T. J., Gombosi, T. I., & De Zeeuw, D. L. (1999). A solution-adaptive Upwind Scheme for ideal magnetohydrodynamics. *Journal of Computational Physics*, 154(2), 284–309. <https://doi.org/10.1006/jcph.1999.6299>

Raeder, J. (2006). Flux transfer events: 1. Generation mechanism for strong southward IMF. *Annales Geophysicae*, 24(1), 381–392. <https://doi.org/10.5194/angeo-24-381-2006>

Ridley, A. J., Deng, Y., & Tóth, G. (2006). The global ionosphere thermosphere model. *Journal of Atmospheric and Solar-Terrestrial Physics*, 68(8), 839–864. <https://doi.org/10.1016/j.jastp.2006.01.008>

Toffoletto, F., Sazykin, S., Spiro, R., & Wolf, R. (2003). Inner magnetospheric modeling with the Rice convection model. *Space Science Reviews*, 107(1), 175–196. <https://doi.org/10.1023/A:1025532008047>

Tóth, G., van der Holst, B., Sokolov, I. V., De Zeeuw, D. L., Gombosi, T. I., Fang, F., et al. (2012). Adaptive numerical algorithms in space weather modeling. *Journal of Computational Physics*, 231(3), 870–903. <https://doi.org/10.1016/j.jcp.2011.02.006>

Villante, U., Recchiuti, D., & Di Matteo, S. (2022). The transmission of ULF waves from the solar wind to the magnetosphere: An analysis of some critical aspects. *Frontiers in Astronomy and Space Sciences*, 9, 835539. <https://doi.org/10.3389/fspas.2022.835539>

Wanliss, J. A., & Weygand, J. M. (2007). Power law burst lifetime distribution of the SYM-H index. *Geophysical Research Letters*, 34(4), L04107. <https://doi.org/10.1029/2006GL028235>

Weigel, R. S., Klimas, A. J., & Vassiliadis, D. (2003). Solar wind coupling to and predictability of ground magnetic fields and their time derivatives. *Journal of Geophysical Research (Space Physics)*, 108(A7), 1298. <https://doi.org/10.1029/2002JA009627>

Xu, S., Liemohn, M. W., Dong, C., Mitchell, D. L., Bougher, S. W., & Ma, Y. (2016). Pressure and ion composition boundaries at Mars. *Journal of Geophysical Research (Space Physics)*, 121(7), 6417–6429. <https://doi.org/10.1002/2016JA022644>

Zhou, H., Turc, L., Pfau-Kempf, Y., Battarbee, M., Tarvus, V., Dubart, M., et al. (2022). Magnetospheric responses to solar wind Pc5 density fluctuations: Results from 2D hybrid Vlasov simulation. *Frontiers in Astronomy and Space Sciences*, 9, 984918. <https://doi.org/10.3389/fspas.2022.984918>